ACCSCIENCE PUBLISHING

Asian Journal of Water, Environment and Pollution

ORIGINAL RESEARCH ARTICLE

Active–passive multichannel analysis of surface waves integration for reconnaissance-scale characterization of shallow limestone bedrock in northern Vietnam

Nguyen Nhat Kim Ngan[1,2]*, Nguyen Xuan Kha[2,3], and Nguyen Thanh Hai[4,5]

[1]Faculty of Physics and Engineering Physics, University of Science, Ho Chi Minh, Vietnam

[2]Vietnam National University, Ho Chi Minh City, Vietnam

[3]Faculty of Geology and Petroleum Engineering, University of Technology, Ho Chi Minh, Vietnam

[4]Institute of Earth Sciences, Ho Chi Minh City, Vietnam

[5]Viet Nam Academy of Science and Technology, Ha Noi, Vietnam

***Corresponding author:**
Nguyen Nhat Kim Ngan
(nnkngan@hcmus.edu.vn)

Citation: Ngan NNK, Kha NX, Hai NT. Active–passive multichannel analysis of surface waves integration for reconnaissance-scale characterization of shallow limestone bedrock in northern Vietnam. *Asian J Water Environ Pollut*. 2026;23(5):026330222. doi: 10.36922/AJWEP026330222

Received: August 10, 2026

Revised: September 3 2026

Accepted: September 3, 2026

Published online: October 10, 2026

Copyright: © 2026 Author(s). This is an Open-Access article distributed under the terms of the Creative Commons Attribution License, permitting distribution, and reproduction in any medium, provided the original work is properly cited.

Publisher's Note: AccScience Publishing remains neutral with regard to jurisdictional claims in published maps and institutional affiliations.

Abstract

Reliable bedrock-depth information is essential for foundation design and seismic site characterization, yet borehole-only investigations provide sparse coverage and active-source surface-wave surveys may lack the low-frequency energy needed to resolve deeper interfaces. This study evaluates co-located active and roadside-passive multichannel analysis of surface waves at three sites in Quang Hanh Ward, Quang Ninh Province, northern Vietnam. Twenty-four 4.5 Hz geophones were deployed at 3 m spacing; active records were generated with a 10 kg sledgehammer, and 32 s passive records were recorded using traffic noise. Normalized frequency-phase-velocity images were combined and inverted to preferred one-dimensional shear-wave velocity (V_S) profiles. Depth-averaged velocities and successive 5 m velocity ratios were compared with two boreholes and Standard Penetration Test data. The combined dispersion information extended from approximately 3 Hz to site-dependent upper limits of about 15–20 Hz and was interpreted to a depth of 50 m. The preferred models show a low-velocity surficial unit (V_S = 164–364 m/s) over a high-velocity unit assigned to fractured limestone (approximately 1,500–2,300 m/s). The principal transition occurs at 10–15 m at Site 1 and 15–20 m at Sites 2 and 3, overlapping borehole evidence that places limestone at approximately 14–16 m. V_{S30} values of 513, 591, and 451 m/s place all three sites in Site Class C under the American Society of Civil Engineers 7-22/International Building Code 2024 and Ground Type B under Eurocode 8. The field example indicates that active–passive integration can extend usable bandwidth while retaining shallow resolution. Because only three lines and two non-blind boreholes were available and inversion uncertainty was not quantified, the proposed velocity-ratio minimum should be treated as a site-specific screening indicator rather than a generally validated bedrock estimator.

Keywords: Active–passive multichannel analysis of surface waves; Shear-wave velocity; Limestone bedrock; Dispersion inversion; Borehole validation

1. Introduction

Near-surface shear-wave velocity (V_S) is a primary descriptor of small-strain stiffness and is widely used in earthquake engineering, foundation assessment, and seismic site characterization.[1,2] Surface-wave methods are attractive because Rayleigh-wave dispersion can be recorded rapidly and non-destructively over a representative ground volume, reducing reliance on spatially sparse intrusive tests.[3,4] The classical multichannel analysis of surface waves (MASW) workflow comprises multichannel acquisition, transformation to a frequency–phase–velocity image, modal picking, and inversion for a layered V_S model.[3,5,6] Engineering applications demonstrate that MASW can identify weak near-surface zones, characterize shallow bedrock, and support site assessment in complex ground.[4,7,8] V_S profiles are particularly valuable where static sampling alone cannot represent the spatial scale controlling wave propagation and foundation response. Repeated or distributed measurements can reveal variability between boreholes, although survey repeatability and lateral heterogeneity must be considered explicitly.[9,10]

Despite its practical appeal, a single acquisition mode rarely provides uniform resolution with depth. Active hammer sources generally provide coherent high-frequency energy and good shallow resolution, whereas passive traffic or ambient sources contribute lower frequencies and longer wavelengths.[11,12] Passive records, however, can be affected by source directionality, near-field energy, and variable source distributions.[13,14] Survey design is therefore a coupled bandwidth-resolution problem in which receiver spacing, spread length, record duration, and usable wavelength content must be considered together.[15–17] Contemporary studies support co-located active–passive acquisition and constrained or joint inversion as practical ways to improve depth coverage.[18–20] Dispersion imaging has also advanced through high-resolution and automated picking methods.[5,21,22] Because multiple layered models may fit similar dispersion observations, probabilistic, uncertainty-aware, and full-wavefield approaches are increasingly important.[23–25] Topography, uneven ground, and source azimuth can further bias one-dimensional interpretations.[26–28] These findings show that a visually continuous dispersion ridge is not, by itself, evidence of a unique subsurface model.

Vietnam's rapid urban and transport development creates strong demand for economical ground characterization, especially where tropical weathering, fractured rock, steep terrain, and karstic limestone complicate interpolation between boreholes. In such settings, an undetected change in rockhead can alter excavation methods, pile length, foundation stiffness, and seismic impedance contrast. International studies show that MASW can support V_S–Standard Penetration Test (SPT) comparison and engineering assessment of weak or heterogeneous ground.[4,29,30] Investigations of bedrock morphology also demonstrate the value of surface-wave information when intrusive control is sparse.[7,9] Peer-reviewed Vietnamese evidence remains limited, although recent studies in M'Drak and Ea Trang have demonstrated the usefulness of MASW and combined seismic methods for weathered-material identification and foundation assessment.[8,31] A clear need therefore remains for field evidence on co-located roadside-passive and active MASW over shallow limestone in Vietnam.

Four gaps motivate the present work. First, few Vietnamese field studies report co-located active and roadside-passive acquisition using an identical linear array, although this configuration can widen usable bandwidth with limited additional deployment effort.[12,20,32] Recent active–passive applications and roadside-processing studies further demonstrate its practical potential.[33,34] Second, bedrock is often inferred from an abrupt V_S increase without adequately reporting modal selection, parameterization, or inversion non-uniqueness.[23,35,36] Third, V_{S30} classification can obscure a shallow, high-contrast bedrock interface because the travel-time average mixes overburden and rock; site-response studies also show that V_{S30} alone does not capture every amplification control.[2,37,38] Fourth, simple depth-averaged velocity ratios have received less validation than probabilistic or joint geophysical approaches.[24,39] A ratio minimum may identify the greatest average-velocity change, but it remains a resolution-dependent screening metric rather than a direct measurement of lithology.

This study therefore aims to (i) integrate active and roadside-passive MASW spectra acquired at three sites in Quang Hanh Ward; (ii) derive V_S profiles to approximately 50 m and characterize the principal stiffness contrast; (iii) compute V_{S30} and depth-averaged V_S at 5 m increments; (iv) test whether the minimum successive average-velocity ratio brackets the limestone interface identified in boreholes; and (v) evaluate the engineering meaning and limitations of the results. The novelty is not the individual MASW components, which are established, but their site-matched integration and the explicit evaluation of a simple 5 m bedrock-screening index against local borehole and SPT evidence in a Vietnamese limestone setting. By separating observed results from interpretive assumptions and by stating uncertainty sources, the study provides a more reproducible basis for subsequent multi-site validation.

2. Materials and methods

2.1. Study area and geological control

The survey area lies in Quang Hanh Ward, Quang Ninh Province, approximately 200 km northeast of Hanoi (Figure 1). It occupies a geological transition between the Hon Gai Formation, dominated by conglomerate, gritstone, and siltstone, and the Bac Son Formation, composed mainly of light- to dark-gray, locally biogenic limestone. Near-surface materials include Quaternary marine deposits with gravel, pebbles, and shell fragments. This juxtaposition creates a strong expected stiffness contrast but also allows localized weathering, fracturing, and lateral variability that can complicate a purely one-dimensional interpretation.

Two boreholes provide the principal geological control (Figure 2). Their logs indicate brownish-gray to reddish-brown clay, locally containing grit, to approximately 14–16 m depth, underlain by dark- to medium-gray limestone that is locally fractured or crushed. SPT *N*-values ranged from 6 to 16 in the clay and reached at least 50 in the limestone. The boreholes were used as point constraints on the lithological boundary depth and were not imposed as fixed layers during MASW inversion. This distinction is important because each seismic profile averages wave propagation beneath a 69 m receiver spread, whereas each borehole samples a narrow vertical column. The comparison is therefore interval-based and supportive rather than a direct one-to-one calibration.

The plan-view map documents the spatial relationship between the three MASW lines and the two boreholes, but the archived files do not preserve surveyed line-to-borehole distances or a unique one-to-one borehole assignment for every site. The comparison was therefore made against the available local borehole control as an interval-level consistency check rather than as independent point validation.

2.2. Survey design and integration logic

Active and roadside-passive MASW data were acquired at the same three sites with the same one-dimensional linear receiver geometry (Figure 3). Co-location limits geometric differences when the two dispersion images are integrated. Active records preferentially sample high-frequency, short-wavelength Rayleigh waves, whereas traffic-generated passive records extend the low-frequency content. The combined workflow consisted of quality control in the time–distance domain, transformation of each dataset to the frequency–phase–velocity domain, normalization on a common grid, integration of the active and passive energy images, modal picking, layered inversion, calculation of depth-averaged V_S, and comparison with borehole and SPT observations. This complementarity follows established active–passive practice,[11,12] including passive-processing studies,[13,14] and is supported by recent integrated applications.[20,32,33]

2.3. Data acquisition

Each line used twenty-four vertical 4.5 Hz geophones connected to a GEODE seismograph (Figure 4). Receiver spacing (Delta x) was 3 m, producing a 69 m spread, and the active-source offset was 12 m. Active Rayleigh waves were generated by repeated impacts of a 10 kg sledgehammer on a metal plate. Traces were stacked in the field until the surface-wave train was visually coherent. The active sampling interval was 1 ms. The archived acquisition

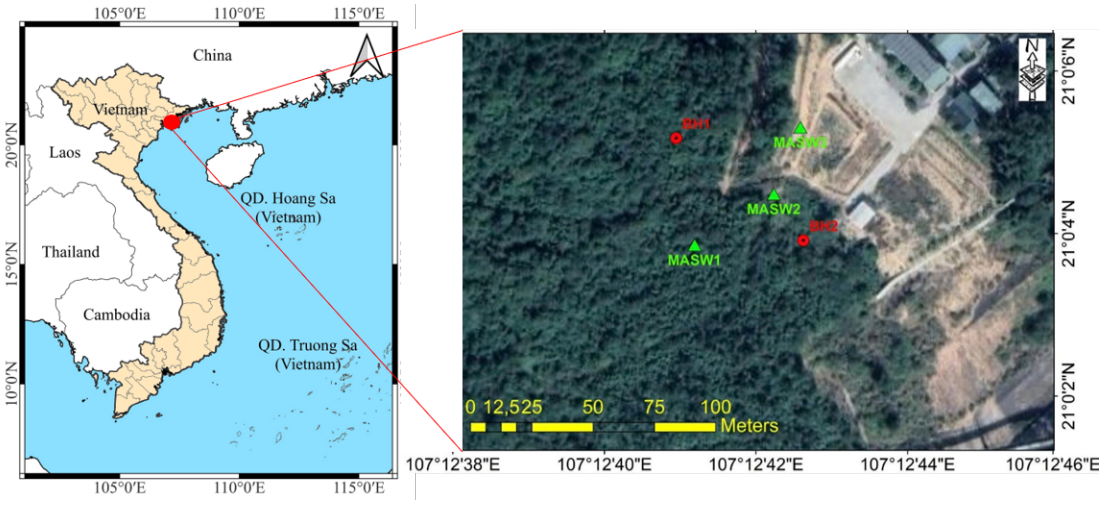

Figure 1. Locations of the three co-located active–passive multichannel analysis of surface waves lines and two geological boreholes in Quang Hanh Ward

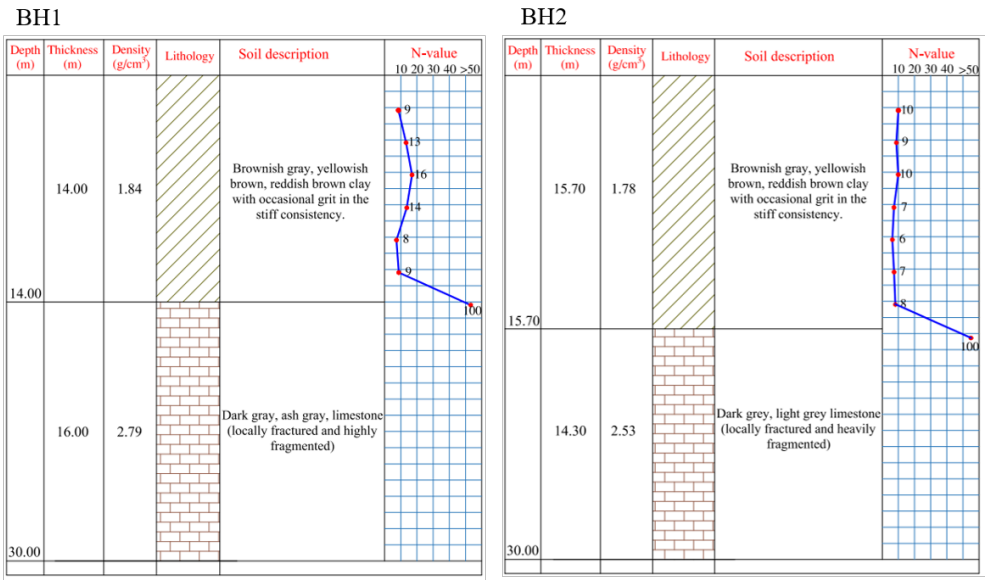

Figure 2. Borehole lithology and Standard Penetration Test results used to validate the interpreted stiffness boundary

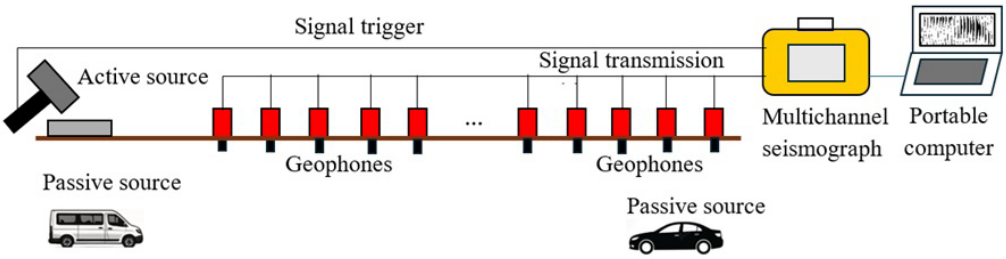

Figure 3. Co-located configurations for active-source and roadside-passive multichannel analysis of surface waves acquisition

description lists a 1 s record length, whereas the plotted active panels in Figure 5 extend to approximately 2 s; this discrepancy could not be resolved from the retained files and should be verified against the raw record headers. The archived field record does not document the number of accepted impacts at each site; therefore, acquisition repeatability and stacking-related signal-to-noise improvement cannot be quantified.

For the roadside-passive survey, the receiver array remained fixed, and road traffic supplied the seismic energy. No hammer or trigger geophone was used. The passive sampling interval was 0.5 ms, and the record length was 32 s, allowing complete vehicle passages to be recorded. Because passive source positions and azimuths were uncontrolled, the wavefield may contain inline-plane, offline-plane, and offline-cylindrical contributions.[12,14] Records were screened visually for persistent dispersive energy rather than interpreted as conventional shot gathers. No quantitative signal-to-noise acceptance threshold or repeat-record statistic was retained; this restricts reproducibility and is considered in Section 4.4. Representative active and passive seismograms from all three sites are shown in Figure 5.

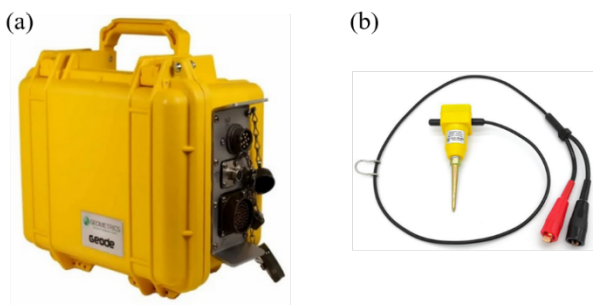

Figure 4. Field equipment: (a) 24-channel GEODE seismograph and (b) 4.5-Hz vertical geophone

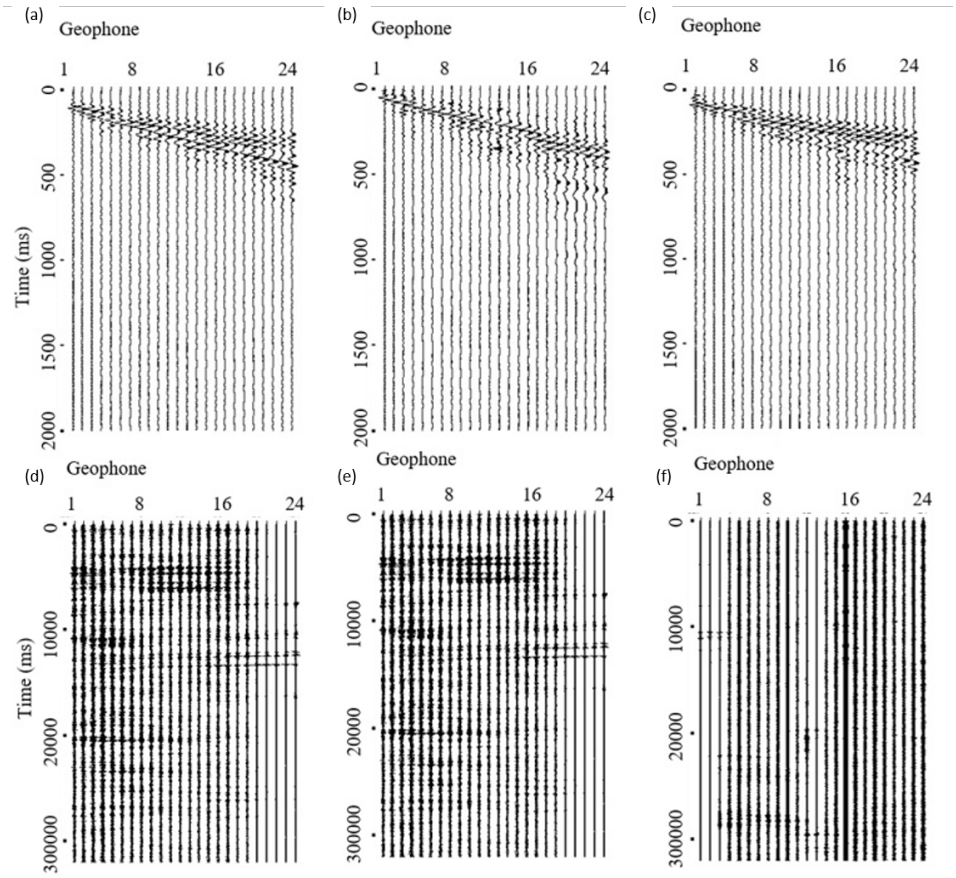

Figure 5. Active-source seismograms (a–c) and roadside-passive seismograms (d–f) at Sites 1–3

2.4. Dispersion imaging and active–passive integration

The recorded time-domain displacement, $u_j(t)$, at each receiver j was first converted to the frequency domain using the Fourier Transform to facilitate spectral analysis (**Equation 1**):

$$U_j(f) = \int_0^T u_j(t) e^{-i2\pi ft} dt \tag{1}$$

where $U_j(f)$ is the complex spectrum at receiver *j*. $u_j(t)$ represents the recorded time-series signal. *f* is the frequency (Hz), and T is the total record length (s). $i = \sqrt{-1}$ denotes the imaginary unit. To generate the dispersion image (phase velocity vs. frequency), a normalized phase-coherence amplitude, *P*(*f*, *c*), was calculated through the phase-shift stacking technique (**Equation 2**):

$$P(f,c) = \frac{1}{N}\sum_{j=1}^{N} \frac{U_j(f)}{|U_j(f)|} \exp\left(i\frac{2\pi f x_j}{c}\right) \tag{2}$$

where N is the total number of receivers in the array. x_j is the distance coordinate of the jth receiver (m). c is the trial Rayleigh-wave phase velocity (m/s).

This formulation transforms multichannel data into a $V-f$ plot, allowing for the identification of experimental dispersion curves (fundamental and higher modes).

To extend the usable bandwidth, the normalized active and passive energy images ($\tilde{D}_a$ and $\tilde{D}_p$) were integrated into a combined dispersion image, $D_c(f,c)$, using a weighted linear combination (**Equation 3**):

$$D_c(f,c) = \frac{w_a \tilde{D}_a(f,c) + w_p \tilde{D}_p(f,c)}{w_a + w_p} \tag{3}$$

where w_a and w_p are the processing weights assigned to the active and passive datasets, respectively. The archived processing record does not retain the numerical active and passive weights; **Equation 3** therefore documents the integration form, and the exact weighting cannot be reconstructed independently from the available metadata.

Although the exact numerical weights were unavailable, the archived processing notes identified the frequency intervals contributing predominantly to the selected combined curves. At Site 1, passive and active data contributed mainly at 2.5–7 Hz and 7–15 Hz, respectively; at Site 2, 3.5–8 Hz and 8–20 Hz; and at Site 3, 3.5–6 Hz and 6–15 Hz. These are contribution ranges rather than sharp filters, and the crossover frequencies indicate where the dominant contribution changes. The corresponding combined accepted ranges were approximately 2.5–15 Hz, 3.5–20 Hz, and 3.5–15 Hz at Sites 1–3, respectively (Table 1).

Integrating the two datasets bridges the frequency gap, combining the high-frequency resolution of active sources with the low-frequency penetration of passive traffic noise.

2.5. Layered inversion and quality criterion

The layered V_S model was derived by minimizing the relative least-squares misfit, $\Phi(m)$, between the observed and calculated phase velocities (**Equation 4**):

$$\Phi(m) = \frac{1}{M}\sum_{k=1}^{M}\left(\frac{c_{obs}(f_k) - c_{cal}(f_k, m)}{c_{obs}(f_k)}\right)^2 \quad (4)$$

where M is the number of frequency samples picked from the dispersion ridge. c_{obs} and c_{cal} are the observed and theoretically calculated phase velocities, respectively. m is the vector of layered model parameters (thickness and velocity).

Dispersion curves were inverted with PS (Park Seismic) version 2.0 using an iterative linearized least-squares approach. The archived processing notes describe a 13-layer parameterization comprising 12 finite layers and a basal half-space. Initial finite-layer thicknesses increased with depth from 0.745 to 8.676 m, and initial V_S increased from 253 to 1,695 m/s. Density (2.071–2.750 g/cm^3) and Poisson's ratio (0.380–0.437) were prescribed by layer and were not independently inverted; P-wave velocity was not treated as an independent inversion parameter. The notes report three iterations. Model selection favored the lowest RMS discrepancy together with geotechnical plausibility and smooth depthwise behavior. Layer-by-layer values, parameter bounds, the numerical convergence threshold, and alternative accepted solutions were not preserved, so the result remains a preferred rather than unique model (Table 2).

The curves picked in **Figures 6–8** were interpreted as the fundamental Rayleigh mode, and this modal assumption was used in inversion. Picks were made manually along the continuous high-energy ridge. No automated mode-crossing test or higher-mode alternative inversion was retained; consequently, the fundamental-mode assignment was treated as an interpretive assumption and a source of model uncertainty. For seismic site characterization, the travel-time averaged V_S to a target depth z, $\bar{V}_{S,z}$, is defined as **Equation 5**:

$$\bar{V}_{S,z} = \frac{z}{\sum_{i=1}^{n(z)} \frac{h_i}{V_{S,i}}} \quad (5)$$

where h_i and $V_{S,i}$ are the thickness and V_S of the ith layer. $n(z)$ is the number of layers within the depth interval z.

When a layer intersects the target depth z, h_i denotes only the portion of that layer lying above z; the travel-time sum therefore terminates exactly at z, including at 30 m for the V_{S30} calculation.

2.6. Depth-averaged velocity, bedrock indicator, and validation

To identify the sharp stiffness contrast at the limestone interface, the successive 5 m average velocity ratio, R_z, was calculated using **Equation 6**:

$$R_z = \frac{\bar{V}_{S,z-5}}{\bar{V}_{S,z}}, z \in \{10, 15, \ldots, 50\}\,\text{m} \quad (6)$$

Table 1. Site-specific frequency contributions and retained software quality indicators

Site	Passive-dominant range (Hz)	Active-dominant range (Hz)	Combined accepted range (Hz)	Software match (%)	Selected-file S/N (%)
1	2.5–7	7–15	2.5–15	82	87
2	3.5–8	8–20	3.5–20	83	91
3	3.5–6	6–15	3.5–15	87	97

Note: Contribution ranges identify the dominant data source and are not sharp filter limits; match and S/N percentages are distinct, software-defined diagnostics.

Table 2. Inversion configuration recoverable from the archived processing notes

Parameter	Available configuration
Software	PS (Park Seismic), version 2.0
Inversion approach	Iterative linearized least-squares
Modal assumption	Fundamental Rayleigh mode; manual ridge picking
Model geometry	13 layers: 12 finite layers plus a basal half-space
Initial finite-layer thickness	0.745–8.676 m, increasing with depth
Initial V_S	253–1,695 m/s, increasing with depth
Poisson's ratio	0.380–0.437; prescribed by layer, not independently inverted
Density	2.071–2.750 g/cm^3; prescribed by layer, not independently inverted
P-wave velocity	Not independently inverted; exact update convention was not retained
Iterations	Three iterations reported in the archived processing notes
Stopping/model selection	Lowest root mean square discrepancy, limited improvement, or maximum iteration; final preference also considered geotechnical plausibility
Unavailable settings	Layer-by-layer starting values, V_S/thickness bounds, numerical convergence threshold, alternative accepted models, and formal uncertainty bounds

A local minimum in R_z indicates the depth interval where the cumulative average stiffness increases most significantly, serving as a proxy for the bedrock head.

3. Results

3.1. Frequency coverage and inversion agreement

The active and passive records contributed complementary portions of the dispersion spectrum. Coherent active energy was concentrated mainly above 5 Hz, whereas the passive records extended the identifiable ridge to approximately 3 Hz. After integration, usable dispersion curves extended from approximately 3 Hz to site-dependent upper limits of about 15–20 Hz, with picked phase velocities from approximately 200 to 2,000–2,300 m/s (Figures 6–8). The observational benefit is therefore an extension of the usable frequency range: active data constrain shorter wavelengths associated with the near surface, while passive data supply longer wavelengths that are more sensitive to the deeper high-velocity unit.

At all sites, the calculated dispersion broadly follows the picked combined curve. The archived processing notes report software match values of 82%, 83%, and 87% for Sites 1–3, respectively. Separate selected-file quality plots show software S/N indicators of 87%, 91%, and 97%. These two sets of percentages represent different software diagnostics. Because their mathematical definitions, residual distributions, and picking-error bounds were not retained, neither was treated as the relative least-squares misfit in **Equation 4** or as evidence of model uniqueness. The profiles were therefore treated as preferred models, and differences among sites were interpreted only where they are consistent with the velocity profiles and available borehole control.

3.2. Two-layer shear-wave velocity structure

The preferred V_S profiles resolve a low-velocity upper unit over a markedly higher-velocity lower unit to the 50-m interpretation depth. The upper unit showed a V_S of 164–364 m/s and a thickness of approximately 14–16 m. These values and depths are compatible with the clay-rich overburden described in the boreholes, where SPT N ranges from 6 to 16. Variability within the upper interval was most evident at Site 2, which had higher depth-averaged velocities than Sites 1 and 3, whereas Site 3 was the softest of the three. The limited number of lines prevents mapping this difference as a continuous lateral feature.

Below the principal transition, V_S rose to approximately 1,500–2,300 m/s. The velocity range was consistent with rock and, in the local geological context, was assigned to the Bac Son limestone. Borehole descriptions of fractured and crushed zones explain why portions of this unit do not require intact-carbonate velocities. The concurrent increase from $N = 6$–16 to $N \geq 50$ supports a major stiffness change, although the SPT refusal-scale response cannot be converted directly into a rock V_S value. The convergent seismic, lithological, and penetration evidence therefore supports the interface interpretation more strongly than any dataset alone.

3.3. V_{S30} and engineering site classification

The calculated V_{S30} values are 513 m/s at Site 1, 591 m/s at Site 2, and 451 m/s at Site 3. These values indicate a relatively stiffer depth-averaged profile at Site 2 and a lower average stiffness at Site 3, within the limitations of three one-dimensional lines. Under ASCE 7-22/IBC 2024 velocity boundaries, all three sites fall within Site Class C. Under Eurocode 8, the same values correspond to Ground Type B because the category names and limits differ (Figure 9; Table 3).[40-41] The classification framework must therefore be stated explicitly; the labels are not interchangeable even though the underlying V_{S30} measurements are unchanged.

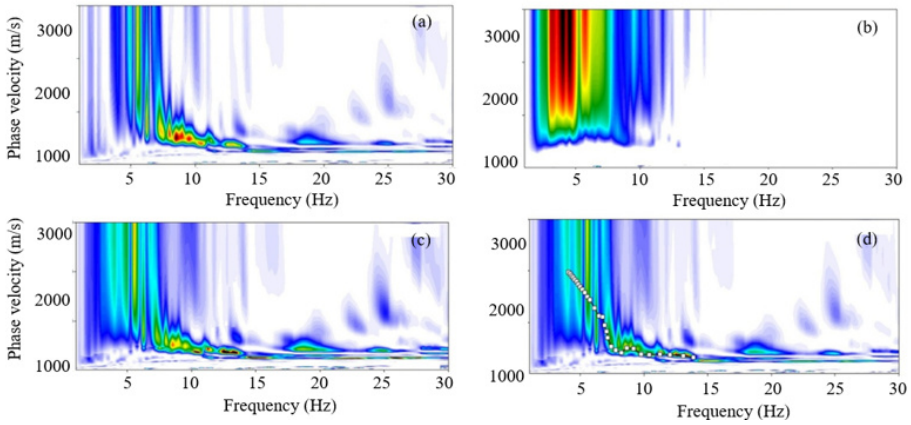

Figure 6. Site 1: (a) active dispersion image, (b) passive dispersion image, (c) combined image, and (d) combined image with manually picked fundamental-mode curve

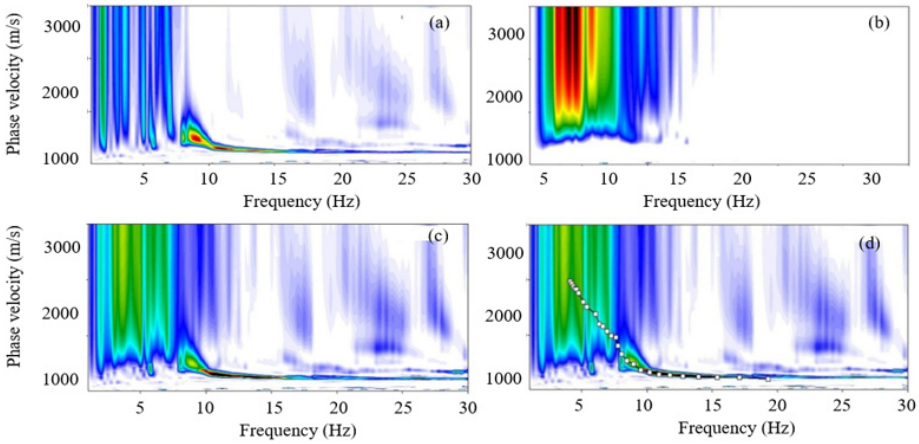

Figure 7. Site 2: (a) active dispersion image, (b) passive dispersion image, (c) combined image, and (d) combined image with manually picked fundamental-mode curve

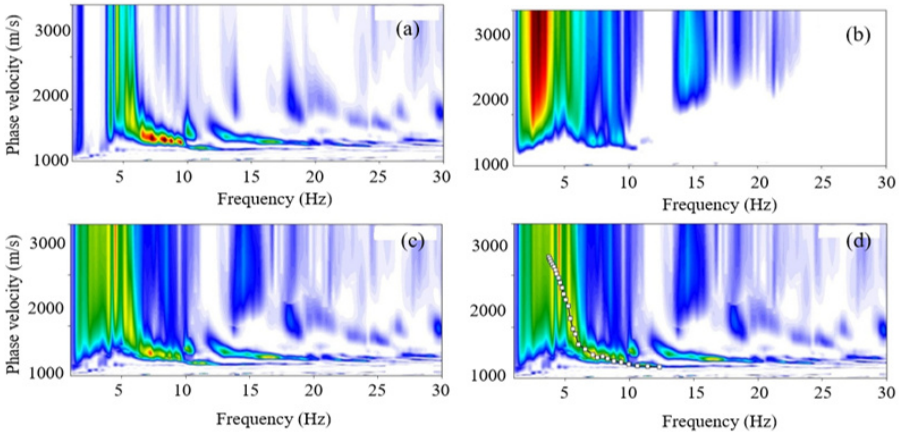

Figure 8. Site 3: (a) active dispersion image, (b) passive dispersion image, (c) combined image, and (d) combined image with manually picked fundamental-mode curve

The depth-averaged curves from 5 to 50 m (Figure 10) increased sharply when the limestone contribution entered the travel-time average. This behavior is expected for a shallow high-velocity substrate. It also shows why V_{S30} alone was insufficient to locate the interface: profiles with different overburden thicknesses can yield similar V_{S30} if their cumulative travel times are comparable. V_{S30} was therefore retained for code-oriented classification, whereas the full profile and borehole comparison were used for geological interpretation.

3.4. Successive velocity ratio and bedrock interval

The successive ratio Rz exhibited the lowest value for the 10–15 m interval at Site 1 and for the 15–20 m interval at Sites 2 and 3 (Figure 11). These minima identified the depth increments that introduced the largest proportional increase in cumulative average V_S. The indicated intervals overlapped the borehole evidence for the top of limestone at approximately 14–16 m. At the resolution used here, the result was therefore an interval match, not an exact point-depth prediction.

Agreement among the ratio minimum, the abrupt profile increase, and the borehole transition supports the utility of Rz as a compact screening index at these sites. Nevertheless, its 5-m resolution was imposed by the calculation interval, and the value depends on the

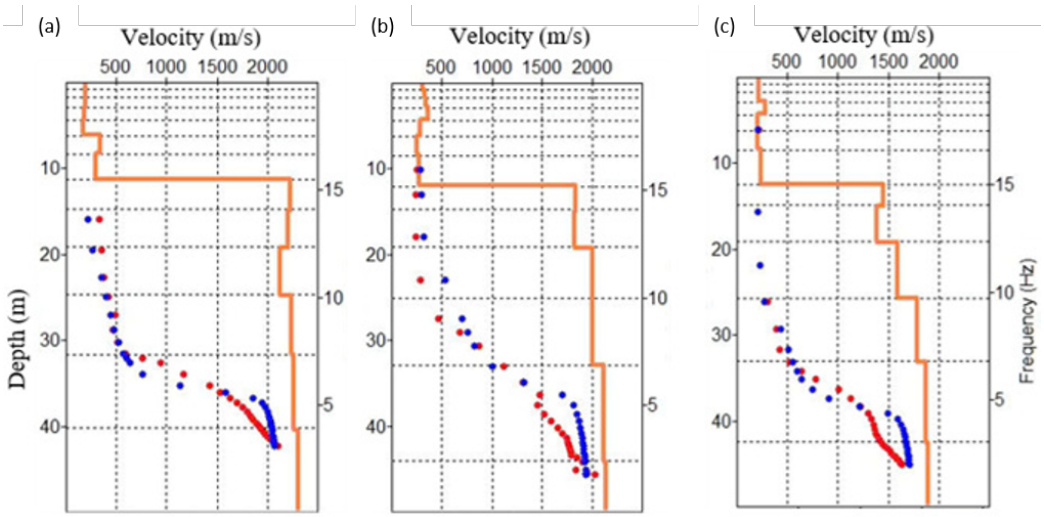

Figure 9. Final one-dimensional V_S profiles at Sites 1–3; blue and red points denote observed (picked) and calculated dispersion, respectively

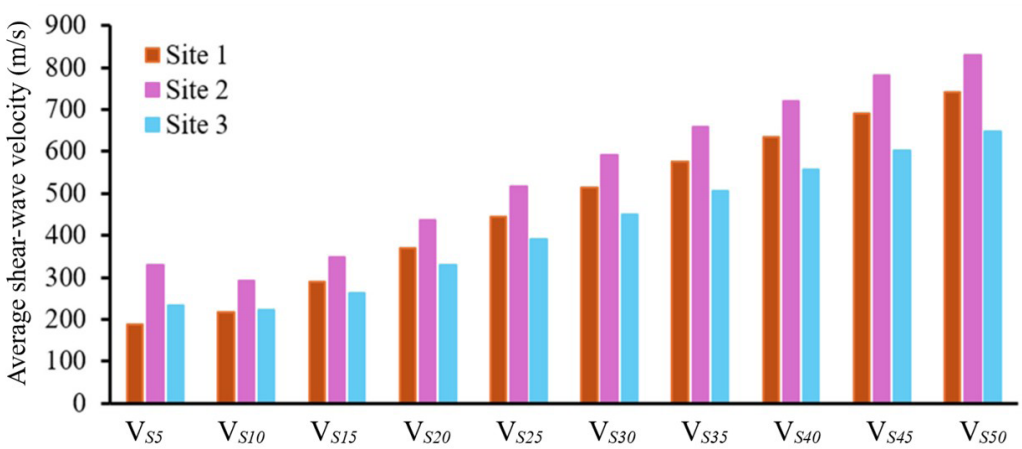

Figure 10. Depth-averaged shear-wave velocity from the surface to 5–50 m at Sites 1–3

Table 3. Site classification of the estimated V_{S30} values under the stated frameworks

Framework	Category	V_{S30} range (m/s)	Site 1 513 m/s	Site 2 591 m/s	Site 3 451 m/s
ASCE 7-22/IBC 2024	Site Class C	>442 to 640	C	C	C
Legacy NEHRP convention	Site Class C	360 to 760	C	C	C
Eurocode 8	Ground Type B	360 to 800	B	B	B

inverted layer model. The result should not be interpreted as demonstrating universal threshold behavior. A larger validation dataset with blind boreholes would be required to estimate sensitivity, specificity, and depth error.

Collectively, the results define a laterally variable but consistently shallow limestone surface beneath clay-rich cover. Site 1 places the strongest transition slightly shallower than Sites 2 and 3, while Site 2 has the highest V_{S30}. These observations answer the study objectives at reconnaissance scale and provide the basis for the mechanistic and uncertainty-focused interpretation below.

4. Discussion

4.1. Reasons why active–passive integration resolves the interface

The observed improvement follows the wavelength dependence of Rayleigh-wave sensitivity. Hammer impacts generate coherent short wavelengths that constrain the low-velocity overburden, but they contribute little energy at the long wavelengths needed to sample below 30 m. Traffic provides longer-duration, lower-frequency energy, extending sensitivity into the limestone. Combining the images on a common grid retains the shallow ridge while reducing the frequency gap between acquisition modes. Active–passive and microtremor combinations likewise improve complementary coverage.[18,20,42] Full-wavefield implementations support the same integration principle,[25] and recent integrated applications provide further field evidence.[32,33]

4.2. Interpretation of the velocity contrast and ratio minimum

The 164–364 m/s upper-unit velocities are typical of soft-to-stiff clayey materials, whereas 1,500–2,300 m/s is compatible with rock. Recent MASW–SPT studies likewise show that increasing penetration resistance is generally accompanied by increasing V_S, although correlations are site-specific and scatter is substantial.[1,29,30] The borehole logs are therefore essential: they convert a geophysical stiffness contrast into a defensible clay–limestone interpretation. The lower-unit range also supports describing fractured or crushed limestone rather than uniform intact bedrock.

The minimum Rz occurs when a 5-m increment first contains enough high-velocity material to change the cumulative travel-time average sharply. Mechanistically, it is a finite-difference indicator of profile curvature, not a direct impedance calculation. Its agreement with the 14–16 m borehole boundary is encouraging, but smoothing, layer parameterization, or a thin high-velocity lens could shift the minimum. Dual-source and constrained inversion studies demonstrate the underlying trade-offs.[19] Probabilistic analyses likewise show that multiple V_S–thickness combinations can fit the same dispersion observations,[23,24] as confirmed by comparative inversion work.[36] Consequently, the ratio should be used to prioritize a depth interval for verification, not to replace drilling.

4.3. Comparison with recent studies and engineering implications

The Quang Hanh profiles are consistent with engineering applications in which MASW identifies weak near-surface zones and shallow bedrock.[4,7] Recent VS–SPT studies also demonstrate the value of surface-wave velocity for geotechnical assessment while emphasizing that correlations are site-specific.[29,30] The present study contributes a Vietnamese limestone field example and shows that passive traffic records can complement an existing 24-channel, 4.5 Hz linear array. This is operationally useful where access, time, or environmental constraints limit intrusive exploration. For engineering design, however, the MASW profiles should support, not replace, site-specific geotechnical investigation. They may guide borehole placement, indicate changes in founding conditions, and provide V_S inputs for response analysis, but bearing capacity and settlement also require strength, density, groundwater, and discontinuity information that was not measured in this study.

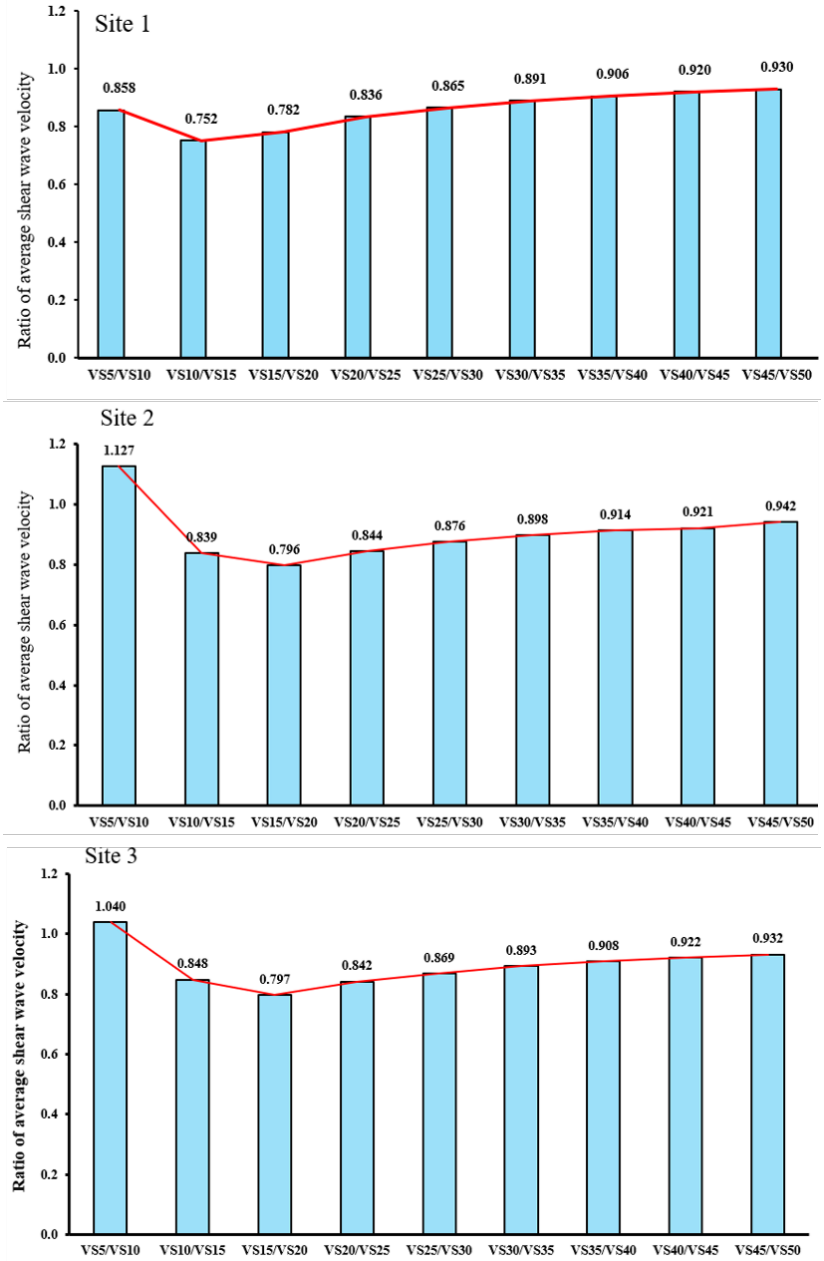

Figure 11. Successive 5-m ratios of depth-averaged shear-wave velocity at Sites 1–3. Labels such as VS10/VS15 denote VS,10/VS,15 and represent the 10–15 m depth interval.

The standards comparison also matters. All sites were Class C under ASCE 7-22/IBC 2024 but Ground Type B under Eurocode 8.[40-41] The physical V_{S30} values were unchanged; only the categorical framework differs. Moreover, V_{S30} averaged across both overburden and rock may not fully represent resonance or amplification where bedrock is shallow.[2,37,38] The full V_S profile, interface depth, and site period should therefore accompany any class label.

4.4. Limitations and priorities for validation

Several limitations constrain generalization. First, the dataset comprised only three one-dimensional lines and two boreholes, so lateral continuity and karst-scale variability cannot be established.[7,9] Topography and uneven ground may also bias a one-dimensional interpretation.[26,27] Second, roadside-passive source position and azimuth were uncontrolled; offline and near-field energy may distort

apparent phase velocity unless directionality is tested.[16,28,34] Third, modal picking was manual and may be subjective near mode crossings or velocity reversals; automated, high-resolution, and multimode methods provide useful sensitivity tests.[22,43,44] Fourth, only preferred inversions and a proprietary match percentage were available. Acquisition repeatability, processing-weight sensitivity, parameterization effects, and probabilistic model ranges were not quantified.[17,24,36] Fifth, the borehole comparison was interval-based and not blinded. The observed overlap therefore demonstrates consistency at these sites but cannot establish predictive accuracy, sensitivity, or specificity.

Future work should repeat active and passive records, document signal-to-noise and wavelength-dependent resolution, invert alternative modal interpretations, and report ensembles rather than a single profile. Joint geophysical methods could improve constraint,[18,19,39] while two-dimensional imaging could test lateral variability. Acquisition sensitivity should be evaluated by changing source offset, passive window length, and subarray aperture; processing sensitivity should vary normalization, modal picks, starting models, and layer numbers. Reporting the accepted model ensemble as median V_S with depth-dependent intervals would make the uncertainty available to designers instead of hiding it in a single curve. The velocity-ratio rule should be calibrated on a larger set of independently logged boreholes using pre-defined depth-error metrics. Blind validation should distinguish whether the first competent-rock contact, the top of fractured rock, or an engineering refusal horizon is the intended target. These steps would convert the present proof of concept into a transferable engineering protocol.

5. Conclusion

This three-site field study provides preliminary evidence that co-located active and roadside-passive MASW can improve usable dispersion bandwidth for reconnaissance of shallow limestone in northern Vietnam. The active data constrained the higher-frequency shallow response, whereas passive traffic records extended the identifiable ridge to approximately 3 Hz. The combined spectra extended to site-dependent upper limits of about 15–20 Hz and supported preferred one-dimensional interpretations to 50 m using a 24-channel linear array. These results demonstrate feasibility at the investigated sites; they do not constitute a general validation of the workflow.

The preferred profiles indicate a strong stiffness contrast between clay-rich Quaternary overburden and a lower high-velocity unit assigned to fractured Bac Son limestone (approximately 1,500–2,300 m/s). The minimum successive 5 m depth-averaged velocity ratio brackets the transition at 10–15 m at Site 1 and 15–20 m at Sites 2 and 3, overlapping the approximately 14–16 m limestone contact in the two boreholes. This agreement supports the use of the ratio as a compact screening indicator at Quang Hanh, but its resolution is fixed by the 5 m calculation interval, and its value depends on the preferred inversion model. The V_{S30} values place all three sites in Site Class C under ASCE 7-22/IBC 2024 and Ground Type B under Eurocode 8, illustrating why the classification framework and the full velocity profile should be reported together.

The principal constraints are the small number of survey lines and boreholes, uncontrolled passive-source direction, incomplete acquisition and processing metadata, manual picking, unavailable inversion ensembles, and non-blind interval validation. The present workflow should therefore be used to prioritize intrusive investigation rather than replace it. A transferable engineering procedure will require repeated acquisitions, documented weighting and inversion settings, uncertainty-aware, two-dimensional assessment of lateral heterogeneity, and blind calibration against a larger borehole dataset using pre-defined depth-error criteria.

Acknowledgments

None.

Funding

This research was funded by Vietnam National University Ho Chi Minh City (VNU-HCM) under a project (grant number CB2025-18-11) within the framework of the program titled "Strengthening the capacity for education and basic scientific research integrated with strategic technologies at VNU-HCM, aiming to achieve advanced standards comparable to regional and global levels during the 2025–2030 period, with a vision toward 2045."

Conflict of interest

The authors declare they have no competing interests.

Author contributions

Conceptualization: All authors
Formal analysis: Nguyen Thanh Hai
Investigation: Nguyen Nhat Kim Ngan, Nguyen Thanh Hai
Methodology: Nguyen Thanh Hai
Writing–original draft: Nguyen Nhat Kim Ngan
Writing–review & editing: Nguyen Nhat Kim Ngan, Nguyen Xuan Kha

Availability of data

Data are available from the corresponding author upon reasonable request.

References

1. Kundu P, Raman D, Pain A, Das J, Sundaram R, Gupta S. Seismic site characterization and development of SPT(N) to shear wave velocity correlation of Noida city. *Sci Rep*. 2025;15(1):12368.

   doi: 10.1038/s41598-025-94502-3

2. Thakur H, Anbazhagan P. Geology, geomorphology and Vs30 based site classification of the Himalayan region using a stacked model. *Eng Geol*. 2025;355:108229.

   doi: 10.1016/j.enggeo.2025.108229

3. Park CB, Miller RD, Xia J. Multichannel analysis of surface waves. *Geophysics*. 1999;64(3):800-808.

   doi: 10.1190/1.1444590

4. Albesher ZI, Alotaibi A, Aljabbab A. Identifying subsurface weak zones in Riyadh, Saudi Arabia, using multichannel analysis of surface wave technique. *J King Saud Univ Sci*. 2025;37:4562025.

   doi: 10.25259/jksus_456_2025

5. Kuang X, Pan Y, Zhang Z, Yuan S. Automatic picking of multimodal Rayleigh-wave dispersion curves from multicomponent data with an energy-density-based clustering method. *Geophys J Int*. 2025;243(1):ggaf323.

   doi: 10.1093/gji/ggaf323

6. Yang XH, Han P, Zhuang J, *et al.* Identification of higher-mode numbers in dispersion curves for Rayleigh wave inversion. *IEEE Trans Geosci Remote Sens*. 2025;63:1-13.

   doi: 10.1109/tgrs.2025.3589016

7. Sgattoni G, Morelli C, Lattanzi G, *et al.* Geophysical investigation and 3D modeling of bedrock morphology in an urban sediment-filled basin: the case of Bolzano (Northern Italy). *Pure Appl Geophys*. 2024;181(6):1871-1893.

   doi: 10.1007/s00024-024-03512-1

8. Nguyen NNK, Le CVA, Vu TM, *et al.* Determination of shear wave velocity using multichannel analysis of surface wave in M'Drak District, Dak Lak Province, Vietnam. *IEEJ Trans Electr Electron Eng*. 2025;20(11):1896-1900.

   doi: 10.1002/tee.70089

9. Chang YH, Tsai CC, Ge L, Park D. Novel method to estimate horizontal variability of shear wave velocity through multichannel analysis of surface waves. *Eng Geol*. 2024;343:107799.

   doi: 10.1016/j.enggeo.2024.107799

10. Ólafsdóttir EÁ, Bessason B, Erlingsson S, Kaynia AM. A tool for processing and inversion of MASW data and a study of inter-session variability of MASW. *Geotech Test J*. 2024;47(5):1006-1025.

    doi: 10.1520/gtj20230380

11. Park CB, Miller RD, Ryden N, Xia J, Ivanov J. Combined use of active and passive surface waves. *J Environ Eng Geophys*. 2005;10(3):323-334.

    doi: 10.2113/JEEG10.3.323

12. Park CB, Miller RD. Roadside passive multichannel analysis of surface waves (MASW). *J Environ Eng Geophys*. 2008;13(1):1-11.

    doi: 10.2113/JEEG13.1.1

13. Cheng F, Xia J, Luo Y, *et al.* Multichannel analysis of passive surface waves based on crosscorrelations. *Geophysics*. 2016;81(5):EN57-EN66.

    doi: 10.1190/GEO2015-0505.1

14. Baglari D, Dey A, Taipodia J. A state-of-the-art review of passive MASW survey for subsurface profiling. *Innov Infrastruct Solut*. 2018;3(1):66.

    doi: 10.1007/s41062-018-0171-2

15. Dal Moro G. MASW? A critical perspective on problems and opportunities in surface-wave analysis from active and passive data (with few legal considerations). *Phys Chem Earth*. 2023;130:103369.

    doi: 10.1016/j.pce.2023.103369

16. Aimar M, Foti S. Near-field effects on the in situ estimation of shear-wave velocity and damping ratio from MASW tests. *J Geotech Geoenviron Eng*. 2026;152(1):06025007.

    doi: 10.1061/jggefk.gteng-14297

17. Adhikari R, Macciotta R, McClymont A, Farrugia J, Deisman N, Hughes S. Managing uncertainties in active MASW: a practical guide for geotechnical engineers. *Geotech Geol Eng*. 2025;43(7):381.

    doi: 10.1007/s10706-025-03342-5

18. Zhao Y, Dutta U, Yang ZJ. Joint inversion of MASW and ambient noise HVSR data for estimating shear wave velocity in warm permafrost sites. *Cold Reg Sci Technol*. 2025;239:104623.

    doi: 10.1016/j.coldregions.2025.104623

19. Ai H, Song X, Zhang X, *et al.* Transdimensional joint inversion of surface wave, refraction, and resistivity data using modified barnacles mating optimizer for near-surface investigations. *J Appl Geophys*. 2025;241:105863.

    doi: 10.1016/j.jappgeo.2025.105863

20. Akın Ö, Sayıl N. Soil characterization in landslide-prone areas using ground shear strain based on active and passive source surface wave methods. *Pure Appl Geophys*. 2025;182(4):1579-1600.

    doi: 10.1007/s00024-025-03696-0

21. Mukherjee S, Bhaumik M, Naskar T. Modified S-transform based high-resolution dispersion imaging method for multi-channel surface wave data. *Soil Dyn Earthq Eng*.

2025;192:109284.

doi: 10.1016/j.soildyn.2025.109284

22. Liu F, Deng B, Su R, Bai L, Ouyang W. DispFormer: a pretrained transformer incorporating physical constraints for dispersion curve inversion. *J Geophys Res Mach Learn Comput*. 2025;2(3):e2025JH000648.

doi: 10.1029/2025jh000648

23. Wang XH, Cao ZJ, Wu T, Du W, Li DQ. Probabilistic inversion of shear wave velocity profile based on the dispersion curve from multichannel analysis of surface waves and inequality constraints on layer thicknesses. *Eng Geol*. 2025;352:108063.

doi: 10.1016/j.enggeo.2025.108063

24. Berti S, Aleardi M, Stucchi E. A probabilistic full waveform inversion of surface waves. *Geophys Prospect*. 2024;72(9):3448-3473.

doi: 10.1111/1365-2478.13595

25. Aimar M, Foti S, Cox BR. Novel techniques for in situ estimation of shear-wave velocity and damping ratio through MASW testing – I: a beamforming procedure for extracting Rayleigh-wave phase velocity and phase attenuation. *Geophys J Int*. 2024;237(1):506-524.

doi: 10.1093/gji/ggae051

26. Vishwakarma P, Bora SS, Prashant A. Variability in receivers responses of MASW test on undulated grounds: a numerical perspective. *J Appl Geophys*. 2024;226:105410.

doi: 10.1016/j.jappgeo.2024.105410

27. Vishwakarma P, Bora SS, Prashant A. Analysis of shear wave velocity estimation using MASW on sloping grounds. *Acta Geophys*. 2024;73(1):359-378.

doi: 10.1007/s11600-024-01382-8

28. Hong Y, Xia J, Zhang H, *et al.* Azimuth correction for passive surface wave dispersion based on polarization analysis. *Geophys J Int*. 2024;238(3):1638-1650.

doi: 10.1093/gji/ggae232

29. Abbas HA, Al-Jeznawi D, Al-Janabi MAQ, Bernardo LFA, Jacinto MASC. Exploring shear wave velocity–NSPT correlations for geotechnical site characterization: a review. *CivilEng*. 2024;5(1):119-135.

doi: 10.3390/civileng5010006

30. Sambath M, Chandrasekaran SS, Maithani S, Ganapathy GP. Seismic site characterization of Coimbatore City, Tamil Nadu, India using the multi-channel analysis of surface waves (MASW) test and correlations between shear-wave velocity and SPT-N. *J Appl Geophys*. 2025;232:105575.

doi: 10.1016/j.jappgeo.2024.105575

31. Nguyen NNK. Deriving geotechnical parameters for foundation design in Ea Trang, Vietnam, through combined seismic methods. *Econ Environ Geol*. 2025;58(4):351-359.

doi: 10.9719/EEG.2025.58.4.351

32. Karslı H, Babacan AE, Akın Ö. Subsurface characterization by active and passive source geophysical methods after the 06 February 2023 earthquakes in Turkey. *Nat Hazards*. 2024;120(6):5257-5286.

doi: 10.1007/s11069-024-06422-6

33. Abdelbaset M, Mohamed A, Sawires R, Omran AAA, Thabet M. Passive and active seismics to identify geotechnical site characterization at industrial zone, Aswan, Egypt. *J Appl Geophys*. 2025;243:105948.

doi: 10.1016/j.jappgeo.2025.105948

34. Philley PD, Taipodia J, Pana T, Anshu AK. Enhancing subsurface imaging: optimization of data acquisition and processing parameters in passive roadside MASW surveys. *Disaster Adv*. 2024;17(10):54-65.

doi: 10.25303/1710da054065

35. Moon SW, Hayashi K, Ku T. Estimating spatial variations in bedrock depth and weathering degree in decomposed granite from surface waves. *J Geotech Geoenviron Eng*. 2017;143(7):04017020.

doi: 10.1061/(ASCE)GT.1943-5606.0001679

36. Yang XH, Zhou Y, Han P, Feng X, Chen X. Near-surface Rayleigh wave dispersion curve inversion algorithms: a comprehensive comparison. *Surv Geophys*. 2024;45(3):773-818.

doi: 10.1007/s10712-024-09826-y

37. Anshu AK, Taipodia J, Kumar SS, Dey A. Seismic site classification of Itanagar city, India, considering spatial variation of shear wave velocity obtained using extensive active MASW survey. *J Appl Geophys*. 2025;243:105981.

doi: 10.1016/j.jappgeo.2025.105981

38. Mazanec M, Valenta J, Málek J. Does VS30 reflect seismic amplification? Observations from the West Bohemia Seismic Network. *Nat Hazards*. 2024;120(13):12181-12202.

doi: 10.1007/s11069-024-06679-x

39. Shi Z, Wang C. Joint inversion of ERT and ambient noise surface wave data with DPC-guided fuzzy c-means clustering for near-surface imaging. *Geophys J Int*. 2024;238(3):1334-1352.

doi: 10.1093/gji/ggae227

40. International Code Council. *2024 International Building Code*. Washington (DC): International Code Council; 2023. https://codes.iccsafe.org/content/IBC2024V2.0

41. European Committee for Standardization. *Eurocode 8: Design of Structures for Earthquake Resistance—Part 1: General Rules, Seismic Actions and Rules for Buildings*. EN 1998-1:2004. European Committee for Standardization; 2004. Accessed August 10, 2026. https://eurocodes.jrc.ec.europa.eu/EN-Eurocodes/

eurocode-8-design-structures-earthquake-resistance

42. Abdelrahman K. Shear wave velocity structure at King Saud University, Saudi Arabia, derived from MASW and microtremor arrays. *Sci Rep*. 2025;15(1):11497.

    doi: 10.1038/s41598-025-90894-4

43. Vantassel JP, Cox BR, Hubbard PG, Yust M. Extracting high-resolution, multi-mode surface wave dispersion data from distributed acoustic sensing measurements using the multichannel analysis of surface waves. *J Appl Geophys*. 2022;205:104776.

    doi: 10.1016/j.jappgeo.2022.104776

44. Vishwakarma P, Prashant A. Hard sandwiched soil layer detection using higher mode in active MASW test. *Geotech Geol Eng*. 2024;42(7):5519-5538.

    doi: 10.1007/s10706-024-02843-z